Small Structures

small structures

www.small-structures.com

RESEARCH ARTICLE OPEN ACCESS

Selective Halide Incorporation in P2-$Na_{0.66}Fe_{1/3}Mn_{2/3}O_2$ Cathodes: Revealing a Compositional Regime for Enhanced Cycling

Anna Domgans[1,2] | Ngoc Thanh Thuy Tran[3] | Sebastian Speer[1,2] | Asghar N. Kayani[4] | Frederik Zantis[1,2] | Tobias Braun[1,2] | Kristian Schaps[1] | Chih-Long Tsai[1] | Hermann Tempel[1] | Luc Raijmakers[1] | Shih-kang Lin[3,5,6,7] | Anna Windmüller[1] | Rüdiger-A. Eichel[1,2]

[1]Institute for Energy Technologies (IET-1 Fundamental Electrochemistry), Forschungszentrum Jülich, Jülich, Germany | [2]Material and Processes of Electrochemical Energy Storage and Conversion, RWTH Aachen University, Aachen, Germany | [3]Center for Resilience and Intelligence on Sustainable Energy Research (RiSER), National Cheng Kung University, Tainan, Taiwan | [4]Department of Physics, Dir. Particle accelerator lab, Western Michigan University, US-Kalamazoo, Michigan, USA | [5]Department of Materials Science and Engineering, National Cheng Kung University, Tainan, Taiwan | [6]Program on Smart and Sustainable Manufacturing, Academy of Innovative Semiconductor and Sustainable Manufacturing, National Cheng Kung University, Tainan, Taiwan | [7]Core Facility Center, National Cheng Kung University, Tainan, Taiwan

Correspondence: Anna Windmüller (a.windmueller@fz-juelich.de)

Received: 10 November 2025 | **Revised:** 6 January 2026 | **Accepted:** 16 January 2026

Keywords: halide anion substitution | Mn/Fe based layered transition metal oxides | Raman spectroscopy | sodium-ion batteries | X-ray diffraction

ABSTRACT

Mn- and Fe-based layered oxides are candidates for sodium-ion battery cathodes due to their high specific capacity and raw material abundance. However, rapid capacity degradation due to irreversible phase transitions during electrochemical cycling is a major challenge. In this study, we explore anionic substitution with A = F^-, Cl^-, and Br^- of $Na_{0.66}Fe_{1/3}Mn_{2/3}O_{2-x}A_x$ (with $x < 0.2$), both experimentally and through density functional theory calculations. We demonstrate that substitution with Cl^-/Br^- is challenged by their larger ionic radii compared to oxygen ions, following the classical Goldschmidt rule. Yet, we reveal the successful aliovalent F^- for O^{2-} substitution with a solubility limit at $x = 0.035$, determined by quantitative phase analysis from powder X-ray diffraction (P XRD), Rietveld refinement, and Raman spectroscopy. Moreover, galvanostatic electrochemical cycling tests on $x = 0.02$ mol F-substituted cathodes showed 15% higher capacity retention after 75 cycles, when compared with the unsubstituted material. Using in situ XRD, we show that the incorporation of F^- alters the kinetics of the P2-P`2 transformation in the low voltage range in favor of the P2 phase. This highlights low-level F-substituted P2-type layered oxides as promising candidates for resource-efficient, high-capacity cathodes in sodium-ion batteries.

1 | Introduction

The global demand for energy has increased significantly since the onset of the industrial age and is accelerating tremendously with the onset of the information age. At the same time, the combustion of fossil fuels as a predominant energy source has been identified as a substantial contributor to global warming, thereby emphasizing the necessity for a transition to environmentally friendly and renewable energy sources such as wind, tidal, hydro, and solar power [1, 2]. However, the integration of renewable energy sources poses significant challenges due to their inherently volatile nature. To ensure a stable and reliable energy supply, the implementation of energy storage systems is imperative. Lithium-ion batteries (LIBs), which rely on Li as the key component, are the current key technology in storing energy from renewable sources. Faced with growing demands, science, industry, and politics worldwide are seeking to diversify energy storage

technologies for better resource availability, lower cost, and tailored performance metrics. As one of the first to enter the mass market, Na-ion batteries (SIBs) are considered the most popular side-by-side technology to LIBs [3].

SIBs allow the replacement of the often used but toxic and costly cathode materials based on Ni, V, and Co in LIBs with more sustainable alternatives such as Fe, Mn, and Al. The decisive factor is the larger ionic radius of Na, which has a significantly better congruence with the ionic radii of Fe/Mn. This ionic radius congruence minimizes lattice strain and facilitates the formation of stable, layered phases. In contrast, the smaller radius of Li in LIB cathodes leads to increased lattice strain in comparable Fe/Mn structures, making their stabilization more difficult. Due to the improved structural compatibility, SIBs therefore allow the use of Fe/Mn-based layered oxides as cathode materials [4–6]. Compared to Ni, V, and Co, these elements not only offer increased sustainability and cost efficiency, but also a significantly lower supply risk [7].

Besides the promising advantages, the development of SIBs faces several challenges, especially in the development of cathode materials. The critical cathode materials properties for battery applications, such as ionic conductivity, Na-ion stoichiometric dependent phase stabilities, transport kinetics, and cycling stabilities, are adversely affected by the much larger ionic radius of Na (0.98 Å) compared to Li (0.69 Å). In addition, the higher mass and higher redox potential of Na/Na^+ compared to Li/Li^+ leads to a lower energy density for SIBs at the cell level. A considerable number of widely recognized LIB cathode materials are incompatible with direct synthesis in the same crystallographic structure for utilization as SIB cathode materials, such as $LiFePO_4$ (LFP) and $LiCoO_2$ (LCO) [8, 9]. In some cases, however, the original structure can be maintained through the process of electrochemical ion exchange, allowing stable cycling of the Na-based material. This finding suggests that structural disparities, in addition to chemical and electrochemical properties of Na and Li, play a pivotal role in determining material compatibility [8, 10].

Current state-of-the art cathode materials for SIBs can be categorized into three classes: polyanions, Prussian blue analogs, and layered transition metal oxides (LTMOs) [5, 7, 11]. The specific capacities of polyanion cathodes are limited to about 80–120 $mAhg^{-1}$ due to their higher molecular weight and lower Na-stoichiometry [12]. In contrast, Prussian blue analogs, such as $Na_xTM[TM(CN)_6]$, have a theoretical specific capacity of 170 $mAhg^{-1}$ [13–15]. Their strong affinity for water not only necessitates more complex synthesis routes and results in lower yield but also significantly reduces their practical specific capacity to $\approx$ 150 $mAhg^{-1}$ [13]. LTMOs have attracted great interest as they can reach high specific capacities from about 110 $mAhg^{-1}$ up to 190 $mAhg^{-1}$ for mixed Ni/Fe/Mn compounds [16]. In addition, LTMOs can be synthesized by a simple solid-state reaction at moderate temperatures between 700°C and 900°C, which makes them feasible for industrial manufacturing [17]. The combination of higher specific capacity and ease of use is a significant advantage that makes LTMOs promising candidates for SIB cathodes [18].

The general formula for LTMOs is Na_xMO_6 (M: Fe, Mn, Ni, Co, Ti). These compounds crystallize in two space groups, i.e. $P6_3/mmc$ and $R\bar{3}m$, depending on Na stoichiometry and synthesis temperature [18]. The polymorphs share similar structural features, consisting of two different layers of Na-ions and MO_6 octahedra. Depending on the Na-ion chemical environment, the Na content in the unit cell, and the stacking order of the layers, the polymorphs are distinct into P2-type and O3-type [19]. In P2-type, the Na-ions are in a prismatic environment, and the Na content is $\leq$0.85 per formula unit (FU), while the Na-ions are in an octahedral environment with a Na content of $0.8 < Na < 1.0$ per FU for O3-type. This leads to a shorter path for Na-ion diffusion in P2-type materials and thus to a better rate performance than O3-type ones [11, 12, 20].

A major disadvantage of LTMOs is irreversible phase transitions during sodation/desodation for both P2-type and O3-type structures, leading to performance degradation due to structural disintegration. In comparison, P2-type LTMOs still offer improved ion conductivity and cycling stability, but layer sliding, upon desodiation, caused by reduced Na content, transitions them to the O2-type structure, which compromises structural stability [21]. O3-type LTMOs, although providing higher initial specific capacities, undergo a more complex sequence of phase transitions, from O3 to (O3 + O′3), then to P3, P′3, and finally to (P′3 + P3″) and P3″, resulting in significant structural decompositions and rapid capacity degradation [17]. As an additional factor, the air sensitivity of O3- and P2-type LTMOs is a major challenge. Both factors, air sensitivity and cycling stability, still restrict the practical applications of both material types [18, 22, 23].

Among the P2-LTMOs, candidates employing TM = Co and Ni exhibit exceptional electrochemical stability. For example, Na_xCoO_2 achieves a capacity of 175 $mAhg^{-1}$ with 82% retention after 300 cycles, while the ternary system $Na_{0.67}Fe_{0.3}Mn_{0.3}Co_{0.4}O_2$ delivers 136.7 $mAhg^{-1}$ with a retention of 85.5% after 100 cycles [24]. Nickel-based systems have demonstrated similar performance. The binary $Na_{0.67}Ni_{0.33}Mn_{0.67}O_2$ demonstrates a capacity of 150 $mAhg^{-1}$ and exhibits a retention of 90% after 100 cycles. The quaternary $Na_{0.67}Ni_{0.33}Mn_{0.57}Cu_{0.05}Mo_{0.05}O_2$ retains 91.5% even after 500 cycles [24]. Further compositions such as $Na_{2/3}Mn_{0.8}Fe_{0.1}Ti_{0.1}O_2$ deliver a capacity of 144.1 $mAhg^{-1}$ at 0.1C with 87.7% retention after 300 cycles between 2 and 4 V [25]. Similarly, $Na_{0.66}Li_{0.18}Mn_{0.71}Ni_{0.21}Co_{0.08}O_2$ achieves 134 $mAhg^{-1}$ at 1C (1.5–4.5 V) and retains 84% of its capacity after 50 cycles [26]. Fe–Mn–O-based systems have comparable initial capacities, for example, 130 $mAhg^{-1}$ for $Na_{0.7}Fe_{0.7}Mn_{0.3}O_2$ [27] and 160 $mAhg^{-1}$ for $Na_{0.5}Fe_{0.5}Mn_{0.5}O_2$ [28], but their performance degrades significantly over time, with retention decreasing to 61.5% and 85%, respectively, after 20 cycles. A similar trend can be observed in systems such as $Na_{1/2}Mn_{1/2}Fe_{1/2}O_2$ (190 $mAhg^{-1}$, capacity retention 79% after 30 cycles at 12 $mAhg^{-1}$ between 1.5 and 4.3 V) [29] and $Na_{2/3}Mn_{2/3}Fe_{1/3}O_2$ (193 $mAhg^{-1}$ capacity retention 79% after 40 cycles at 12 $mAhg^{-1}$ between 1.5 and 4.3 V) [30], where the initial high capacities decrease noticeably during increasing cycle numbers. Compared to the layered oxides containing Ni and Co, the binary Fe/Mn layered oxides exhibit the atypical phenomenon of a strong degradation of capacity, which considerably limits their practical application.

Anionic substitution, particularly with the halide ion F^-, has been shown to be an effective method of suppressing or delaying phase transitions and thereby increasing structural stability by strengthening the bonds within the structure and producing a more stable crystal lattice, leading to enhanced cycling stability [31, 32]. For example, $Na_{0.67}Ni_{0.33}Mn_{0.67}O_{1.95}F_{0.05}$ exhibits a

remarkable increase in cycling stability at 340 $mAhg^{-1}$, with a capacity retention of 95% after 400 cycles, compared to 88% capacity retention of the unsubstituted counterpart [33]. Similarly, $Na_{0.60}Ni_{0.30}Mn_{0.70}O_{1.95}F_{0.05}$ [34] exhibits 15–20% higher specific capacity than the unsubstituted one, while $Na_{1.2}Mn_{0.80}O_{1.50}F_{0.50}$ achieves an impressive capacity retention of 90% after 300 cycles, which is much higher than only 70% for the unsubstituted one [35]. Furthermore, as F-substituted represents a critical strategy for optimizing SIB cathodes, other halides substituent such as Cl^- and Br^- represent a promising alternative. These elements may be more attractive than F^- in terms of environmental impact, abundance, and lower toxicity. The potential benefits of Cl^- and Br^- substitution are not yet explored and may open new ways to optimize the electrochemical performance of SIBs.

To fill the gap, this study explores halide substitution (F, Cl, Br) as a strategy to enhance the structural stability and electrochemical performance of the P2-type cathode material $Na_{0.66}Fe_{1/3}Mn_{2/3}O_2$. To study the effects of halide substitutions, we use a combined experimental and theoretical approach through synthesis conditions close to thermodynamic equilibrium and density functional theory (DFT) calculations. Furthermore, samples that could successfully be synthesized with incorporated halide-anion will be subjected to extended electrochemical analysis to validate and benchmark their performances against the unsubstituted P2- $Na_{0.66}Fe_{1/3}Mn_{2/3}O_2$.

2 | Results and Discussion

2.1 | Synthesis and Characterization of Halide Substituted $Na_{0.66}Fe_{1/3}Mn_{2/3}O_2$

Aliovalent substitution of halide anions ($A = F^-$, Cl^-, Br^-; $x = 0.02$, 0.05, 0.1, 0.2 mol) for O^{2-} in P2-$Na_{0.66}Fe_{1/3}Mn_{2/3}O_{2-x}A_x$ (Figure 1a) was performed via solid-state reaction, from oxide and halide precursors at 900°C in air [33, 36]. The applied synthesis route resulted in fine-grained powders with irregular particle shapes, as can be seen in the scanning electron microscope (SEM) images in Figure 1b–e. The NFMO sample (Figure 1b) shows a large number of well-crystallized primary particles (grains) that exhibit a characteristic platelet-like morphology, with grain diameters around ~3 µm and heights of ~1 µm. In addition, a small number of larger particles exceeding 5 µm are dispersed among the finer grains. The 0.02 mol F-substituted sample (Figure 1c) resembles the microstructure of the unsubstituted powders in terms of morphology, but its primary particle size is smaller (the same is observed for the 0.05 and 0.1 mol F-substituted samples (Figure S1, Supporting Information). Upon substitution with Cl^- or Br^-, the particle size further decreases to approximately 1 µm or smaller, accompanied by a noticeable reduction in the number of larger particles (Figure 1d,e). Higher substitution levels increase the number of larger particles significantly (Figure S1, Supporting Information). Interestingly, agglomerates of small, nonplatelet-like particles are observed in 0.2 Br-substituted NFMO, which could already be an indication of unsuccessful substitution of Br^- into the NFMO structure, given that the characteristic platelet-shaped morphology of the main material is not visible. The SEM images indicate that the shape and size of the particles of NFMO are consistent with the platelet-like particles reported in previous studies of NFMO synthesized by solid-state reaction at 900°C [37]. The EDS analyses of the SEM images (Figure S2, Supporting Information) confirm that NFMO exhibits a uniform distribution of the elements Na, Fe, Mn, and O throughout the sample. Furthermore, F^- is distributed homogeneously in the F-substituted samples (NFMF0.02, 0.05, 0.1). However, in sample NFMF0.2, the presence of distinct bright areas in the Na and F maps suggests the formation of a Na/F-rich secondary phase. In the Cl- and Br-substituted samples (0.02 and 0.2), the overall element distribution remains largely homogeneous. Whereas NFMCl0.02 and NFMBr0.2 exhibit localized bright spots in

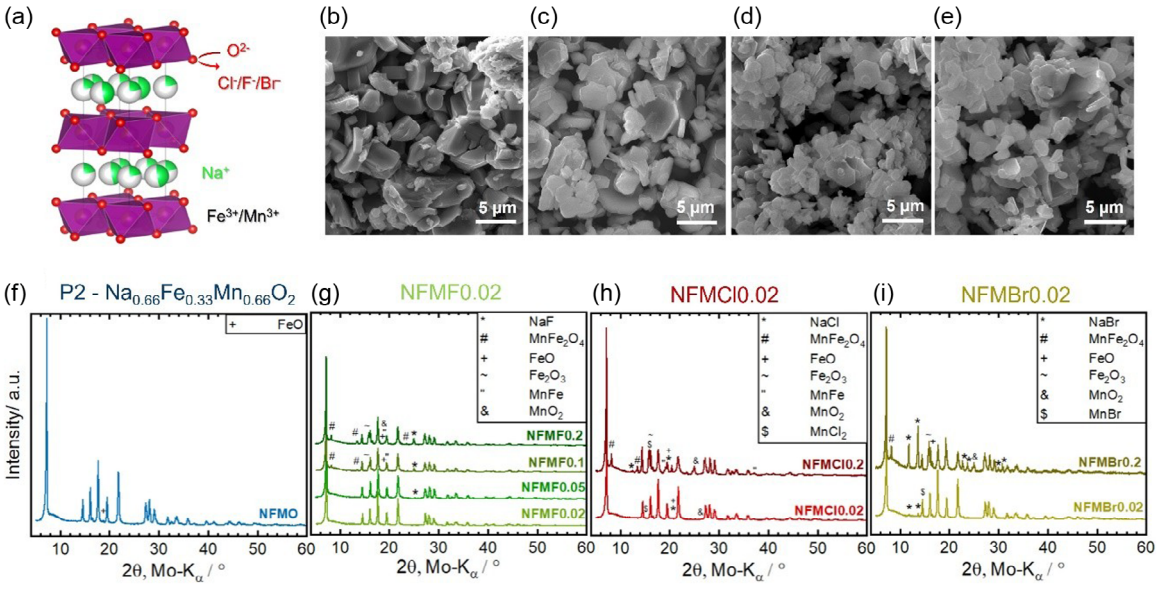

FIGURE 1 | Structural scheme of layered transition metal oxide (a). SEM image of NFMO (b), 0.02 mol F-substituted NFMO (c), 0.02 mol Cl-substituted NFMO (d) and 0.02 mol Br- substituted NFMO (e). PXRD-pattern of NFMO (f),0.02 mol F-substituted (g), 0.02 Cl-substituted (h) and 0.02 Br-substituted (i) materials.

the Cl and Br maps, respectively, which could suggest the presence of halide-rich secondary phases and unsuccessful incorporation. We further confirmed bulk chemical compositions with inductively coupled plasma optical emission spectrometry (ICP-OES), confirming that the targeted stoichiometries were achieved, with deviations of ±0.00923 mol Na and ±0.00801 mol Mn per FU, assuming Fe = 0.33 mol per FU (Table S1, Supporting Information).

For qualitative phase analysis of the sample series, powder X-ray diffraction (PXRD) measurements were performed for both NFMO and halide-substituted NFMO samples. Figure 1f–i compares the diffraction patterns of P2-$Na_{0.66}Fe_{1/3}Mn_{2/3}O_{2-x}A_x$, where A = F^-, Cl^-, Br^- and $x = 0.02$, 0.05, 0.1, and 0.2 mol. NFMO crystallizes in a hexagonal structure with space group *P6₃/mmc* (Figure S3, Supporting Information), in good agreement with previously reported data [30, 38]. A minor reflection at 18.84° 2θ is observed, which can be attributed to a small amount of FeO as a secondary phase. The diffraction patterns of the F-substituted NFMO series reveal a progressive increase in secondary phase fractions with increasing F^- content. At a substitution level of $x = 0.02$ mol, the pattern indicates a phase-pure material. However, at $x = 0.05$, a distinct reflection at 25.01° appears, corresponding to NaF. With further increase to $x = 0.1$, multiple secondary phases are detected, including Mn_2FeO_4 (7.84° and 13.61°), Fe_2O_3 (16.00°), FeO (19.08°), MnFe (19.18°), and NaF (25.35°). At the highest F^- concentration studied ($x = 0.2$), additional reflections indicate further phase segregation, with Mn_2FeO_4 (8.24°, 13.32°), Fe_2O_3 (16.05°), FeO (19.04°), MnFe (19.29°), NaF (25.16°), and a newly observed MnO_2 phase at 18.44°.

The PXRD pattern of the 0.02 mol Cl-NFMO sample reveals the formation of several secondary phases. A reflection at 15.27° is attributed to $MnCl_2$, followed by peaks at 20.52° and 20.77°, corresponding to NaCl and FeO, respectively. Additionally, a peak at 26.63° indicates the presence of MnO_2. For the 0.2 Cl-NFMO sample, a more complex diffraction pattern is observed, with reflections at 8.11° and 13.62° corresponding to Mn_2FeO_4. A peak at 12.73° is assigned to NaCl, while further reflections at 15.67° ($MnCl_2$), 15.87° (Fe_2O_3), and 18.97° (FeO) indicate additional secondary phases. At 19.17°, a reflection consistent with MnFe is detected, followed by another NaCl peak at 20.47°. Finally, reflections at 24.98° and 26.63° confirm the presence of MnO_2. Similar to the Cl-substituted NFMO samples, the Br-substituted samples also show clear evidence of secondary phase formation. In the 0.02 Br-NFMO sample, reflections are observed at 11.87° and 13.72°, corresponding to NaBr, and at 14.57°, attributed to MnBr. At a higher substitution level of $x = 0.2$ mol, the PXRD pattern reveals additional and more intense reflections. Peaks at 8.21°, 12.02°, and 13.67° are consistent with $MnFe_2O_4$ and NaBr, while a reflection at 15.87° indicates the presence of Fe_2O_3. Further peaks at 16.52° and 25.08° are assigned to FeO and MnO_2, respectively. Subsequent substitution with higher concentrations and various halides resulted in the observation of several secondary phases, indicating an overall metastable and segregating system. The coexistence of FeO with the layered P2-type material (and other coexisting phases, such as MnFe) in thermodynamic equilibrium is further substantiated by the observation of significant FeO mass fractions at higher substitution degrees, for example, in NFMBr0.2. Due to the locally limited oxygen supply during the sintering process, locally reducing conditions may occur, favoring the formation of a metallic MnFe phase and reduction to FeO.

In summary, the diffraction pattern of the 0.02 mol F-substituted NFMO sample indicates successful fluoride incorporation at this level, as no extra reflections are detected. In contrast, the presence of several secondary phases in samples with higher F^- content and in all Cl- and Br-substituted samples suggests that halide incorporation was either incomplete or unsuccessful under the applied solid-state synthesis conditions.

2.2 | Quantitative Phase Analysis of $Na_{0.66}Fe_{1/3}Mn_{2/3}O_{2-x}A_x$ (A = F^-, Cl^-, Br^-)

Quantitative phase analyses (QPA) based on PXRD was performed for all samples (Figures 2a,b, S4 and S5 (Supporting Information)). P2-NFMO (ICSD code 231006) with the hexagonal space group $P6_3/mmc$ was used as a starting model for the QPA and Rietveld refinement [38, 39]. Lattice parameter, size, and strain were determined using the Pawley method [40]. In the Rietveld refinement analysis for NFMO (Figure S4a, Supporting Information) and all F/Cl/Br-substituted NFMO (Figures S4b and S5, Supporting Information), the scale factor, thermal Debye–Waller factors, and occupancies were refined (all parameters are provided in Supporting Information Tables S2–S7). The analysis for NFMO indicates an almost phase-pure material with only a small fraction of FeO (0.48 wt%) (Figure S4a, Supporting Information). The lattice parameter refines to $a_{hex} = 2.91980(6)$ Å and $c_{hex} = 11.1647(4)$ Å. A value of 1.9701(13) Å for the bond length of M–O (M: Fe/Mn) is calculated (Table S2, Supporting Information). This is similar to the reported lattice parameters for P2-$Na_{0.66}Fe_{1/3}Mn_{2/3}O_2$ from Mortemard de Boisse et al. and Zhao et al., which reported lattice parameters in the range of $a_{hex} = b_{hex} = 2.94$–2.91 Å and $c_{hex} = 11.18$–11.27 Å [30, 38].

The 0.02 mol F-substituted NFMO is a phase-pure material without apparent secondary phases (Figure 2a). The lattice parameters increase to $a_{hex} = 2.92732(5)$ Å and $c_{hex} = 11.1842(3)$ Å, as well as the M—O bond length increases from 1.9701(13) Å to 1.9802(11) Å, Table S3. For 0.02 mol Cl- NFMO yields secondary phase fractions of 0.67 wt% NaCl, 0.30 wt% $MnCl_2$, 0.25 wt% FeO and 0.21 wt% MnO_2 (Figure 2b). The lattice parameter $a_{hex} = 2.91887(6)$ Å for the main phase remains the same compared to NFMO, while $c_{hex} = 11.2096(4)$ Å increases by 0.0449 from that of NFMO, Table S4. The TM—O bond length increases slightly to 1.9707(13) Å. The QPA of the 0.02 mol Br-substituted NFMO shows that 1.25 wt% NaBr and 0.30 wt% $MnBr_2$ are present in the sample (Figure S4b, Supporting Information). The lattice parameters increase to $a_{hex} = 2.92760(6)$ Å and $c_{hex} = 11.1930(5)$ Å, Table S6. For all higher halide substitutions, multiple secondary phases, such as Na halides and different TM-oxides, are formed in each sample, Figure S5 (Supporting Information). Figure 2c shows an overview of the phase fractions determined by QPA for all samples, while detailed values are provided in Table S7 (Supporting Information).

The QPA indicates that halides preferentially interact with Na, leading to the formation of TM-O secondary phases rather than halideincorporation into the NFMO phase. Thus, a halide-substituted P2 phase without coexisting secondary phases cannot be achieved, and only the 0.02 mol F-substituted sample displayed phase purity in PXRD. However, the absence of crystalline

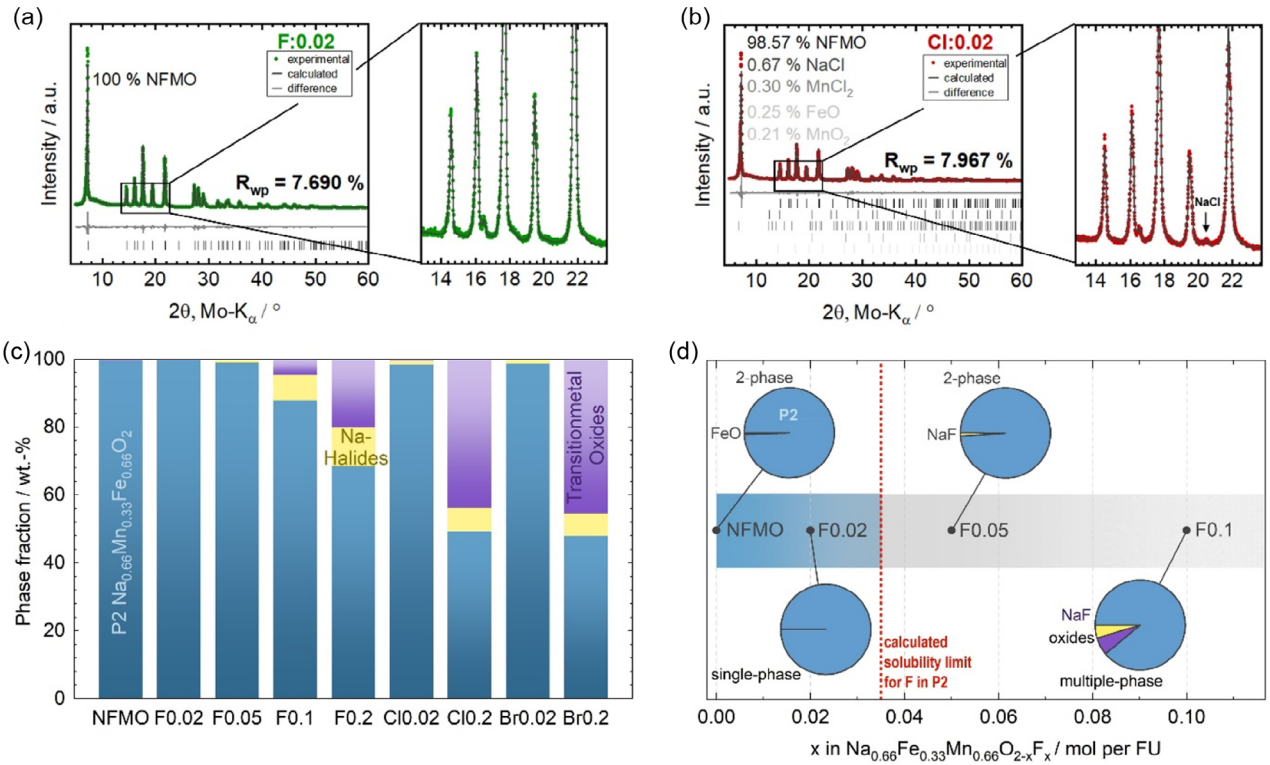

FIGURE 2 | Rietveld refinement results for the sample series. Examples of fits for 0.02 mol F-substituted (a) and 0.02 mol Cl-substituted (b) materials (inspect SI Figures S3 and S4 for complete series). Determined phase fraction of samples from QPA and ICP-OES (c). Solubility limit of F-substituted samples (d).

secondary phases in PXRD patterns is not a stand-alone proof of successful incorporation of a substituent.

Typically, successful substitution gets evident from changes in the lattice parameters along the substitution series. In our case, however, the varying Na content within the samples, as confirmed by ICP-OES (Table S1, Supporting Information), results in changes to the valences of Fe and Mn due to charge compensation. The changes in the lattice parameters are influenced by these different ionic radii of the transition metals. As the Na content decreases, the combined valence of Fe and Mn ions increases, which leads to a smaller average ionic radius and consequently to a reduction in the lattice parameter. For all 0.02 mol F/Cl/Br-NFMO samples, the Na content is higher than that of NFMO, which is consistent with an increase in the a_{hex}/c_{hex} lattice parameter. A comparison of the lattice parameters determined by Rietveld refinement analysis with the Na stoichiometries calculated in each case from QPA and Rietveld analysis reveals a clear correlation between the Na content in the P2 phase and the lattice parameters (Figures S6 and S7, Supporting Information). Therefore, in this study, we refrained from validating the success of F-substitution based on changes in lattice parameters. Instead, we verified the incorporation of F^- through QPA and by using additional techniques in the following sections.

To understand F^- incorporation in NFMO, we attempt to calculate the solubility limit of F^- in NFMO on the basis of the detected weight fraction of secondary phases in PXRD. The solubility limit is defined as the maximum concentration of a component (in this case, F^-) in a phase (in this case, NFMO) before secondary phases form. On the basis of the lever rule, the mass fraction of F^- in the NFMO phase (w_F^{NFMO}) can be calculated from the mass fraction of F^- in the secondary phase NaF (w_F^{NaF}), the total mass of F^- in the sample (w_F^{total}), and the mass fraction of NaF in the sample (w^{NaF}) for a two-phase system consisting only of NaF and NFMO as:

$$w_F^{NFMO} = \frac{w_F^{total} - w^{NaF} \cdot w_F^{NaF}}{1 - w^{NaF}} \quad (1)$$

Figure 2d shows the calculated solubility limit of F^- in the P2-NFMO. We calculated the solubility limits for F^- in NFMO based on the F 0.05 mol and F 0.1 mol sample where NaF secondary phase fractions were detected and quantified to 1 wt% and 6.3 wt% respectively. Equation (1) thus yields 0.04 mol F^- per FU in the NFMO phase for the F^- 0.05 sample and 0.03 mol F^- per FU in the F 0.1 mol sample. Rutherford backscattering spectrometry (RBS) measurements (Figure S8, Supporting Information) were used to quantify F- and the elements Na, Fe, Mn, O^{2-} in F-substituted samples and to exclude a possible loss of F^- and thus confirm the solubility limit. While F^- was only clearly detected in the 0.1 mol sample (1.5 at%), its absence in the 0.05 mol sample suggests a concentration below the detection limit (~0.5 at%). Nevertheless, the detection in the higher substituted sample indicates that F^- was successfully incorporated, and it is reasonable to assume its presence in all F-substituted samples. We thus found ~0.035 mol F^- per FU as the solubility limit in the NFMO phase. This indicates successful incorporation of F^- into NFMO for F 0.02 mol, obtaining a single phase $Na_{0.66}Fe_{0.33}Mn_{0.66}O_{0.98}F_{0.02}$.

2.3 | Raman Spectroscopy

Raman microspectroscopy was used to investigate the change in bond strengths as a function of anionic substitution. The five expected active Raman modes ($E_{1g} + 3E_{2g} + A_{1g}$) for P2-NFMO [30, 34, 37, 41] are observed in the spectra of both the pristine and 0.02 mol F/Cl/Br-substituted NFMO samples (Figure 3a–d). The spectra were successfully deconvoluted using Voigt functions to accurately determine the band positions and band width of individual vibrations. The fitting results show that the band position of the A_{1g} vibration in NFMO and in 0.02 mol Cl-substituted NFMO are at 637.7 cm^{-1} and 637 cm^{-1}, respectively. The full width at half maximum (FWHM) of A_{1g} increases slightly by 3.03 cm^{-1} wavenumbers from 34.83 cm^{-1} for NFMO to 37.86 cm^{-1} for 0.02 mol Cl-substituted NFMO. In contrast, the 0.02 mol F-substituted NFMO shows a significant blue shift to 639 cm^{-1} with a peak broadening of 8.96 cm^{-1} in comparison to the unsubstituted NFMO, which indicates a change in bond strength.

If we assume F^- is substituted directly onto the O^{2-} site by aliovalent substitution, an increase in bond strength and resulting blue shift can be expected, as well as a decrease in the lattice parameter along the *c*-axis, since F^- is more electronegative than O^{2-}. The increase in bond strength should impact the observable optic modes in Raman spectroscopy. Furthermore, the replacement of F^- by O^{2-} would lead to a reduction of the TM ions to compensate charges and induce local distortions into the given coordination symmetry, leading to a broadening of Raman bands [33]. The fitted Raman spectra for NFMO and the 0.02 Cl- and F-substituted samples reveal a blueshift of 1.3 cm^{-1} and 2 cm^{-1}, respectively, along with peak broadening of the A_{1g} mode in the F-substituted sample, indicating successful F^- incorporation and ineffective Cl^- substitution. The A_{1g} mode, associated with out-of-plane M–O (M = Fe/Mn) stretching along the *c*-axis, is more sensitive to mass and bond strength changes than the in-plane E_{2g} bending mode [30, 34, 38, 42]. Although Rietveld refinements show no lattice contraction, this is likely due to increased Na content rather than unsuccessful F^- incorporation.

The absence of band shifts in Cl^- substituted samples aligns with QPA results, confirming the unsuccessful Cl^- incorporation, while the 0.02 mol Br-substituted sample (Figure 3d) shows a very inhomogeneous spatial distribution of local chemical order as apparent from the Raman spectroscopic mapping sampled in an area of 50 µm by 50 µm. Specifically, the ratio of the A_{1g} mode of component 1 appears at 637.4 cm^{-1} with a FWHM of 41.46 cm^{-1}, while for component 2, it is located at 634.34 cm^{-1} with a FWHM of 28.57 cm^{-1}. In component 1, the A_{1g} position remains unchanged, but the band exhibits broadening compared to NFMO. In contrast, component 2 shows a redshifted A_{1g} mode with a narrower band. A similar inhomogeneities are observed at all higher substitution concentrations (Figure S9, Supporting Information).

As QPA revealed that increasing halide concentration destabilizes the P2-NFMO main phase and promotes the formation of TM-oxide and Na/TM-halides secondary phases, local compositional

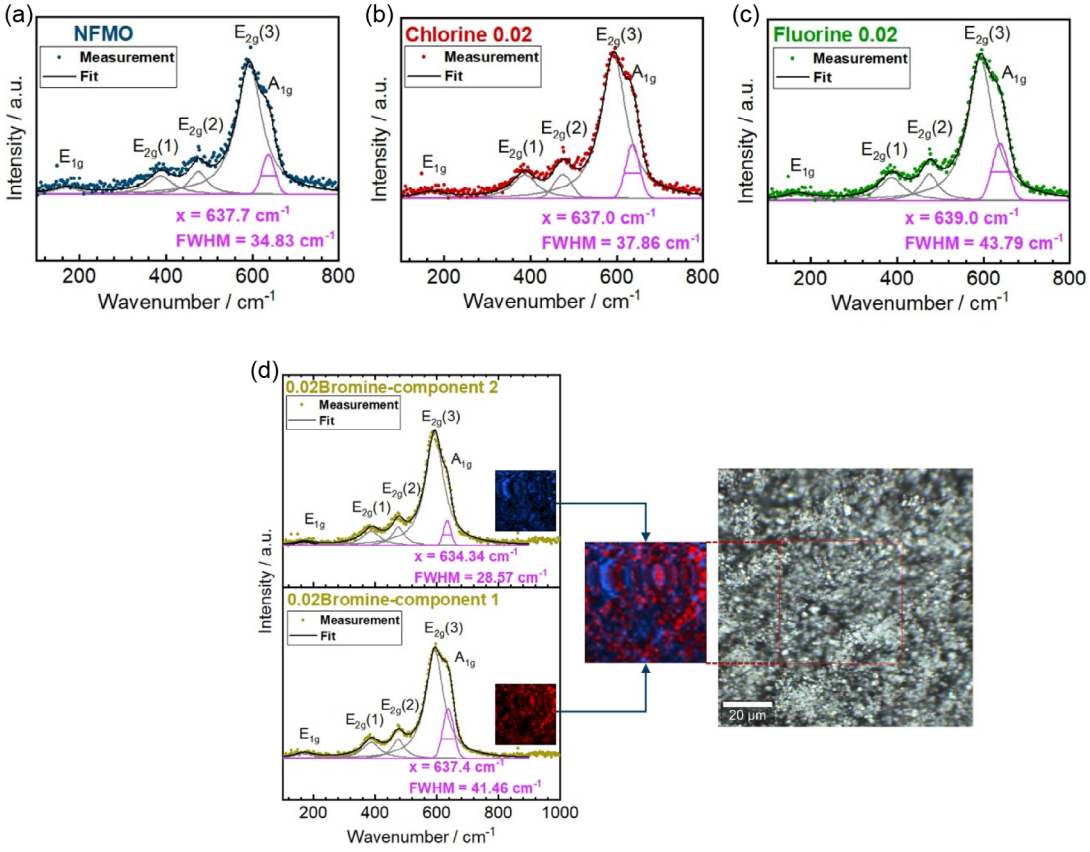

FIGURE 3 | Raman measurement and fit with Voigt function of P2-NFMO (a), 0.02 mol Cl-substituted NFMO (b) and 0.02 mol F-substituted NFMO (c). Results of Raman mapping for 0.02 mol Br-substituted NFMO and its optical image of measured area (d).

variations in Na, Fe, Mn, and O within the destabilized P2-NFMO may emerge, resulting in a broader distribution of Fe/Mn–O (A_{1g}) vibrational environments [42].

This interpretation is further supported by literature reports on NaF secondary phases, in which only second-order Raman bands are observed, indicating the absence or very low intensity of first-order fundamental modes [43]. Consequently, for F $x > 0.02$ in this system, the Raman activity of the NaF secondary phase is inherently weak, making the detection of clearly defined first-order peaks unlikely. Similarly, studies on $MnCl_2 \cdot 2H_2O$ suggest that crystalline $MnCl_2$ exhibits only weak Raman scattering, with the detectable modes being limited to low wave numbers. This probably explains the absence of clear Raman signatures from $MnCl_2$ or similar secondary phases in the substituted NFMO samples [44]. Instead, subtle effects such as bandwidth broadening or splitting at higher F/Cl/Br concentrations can indirectly indicate the formation of a secondary phase.

The results from QPA and Raman are consistent with Goldschmidt's rules, which predict that ionic substitution in a crystal lattice is feasible when the substituting ions differ in radius by less than ~15% and possess similar charges to maintain charge neutrality. F^-, with an ionic radius of 1.33 Å (VI), closely matches that of O^{2-} (1.40 Å (VI)), enabling direct substitution. In contrast, the significantly larger radii of Cl^- (1.81 Å(VI)) and Br^- (1.96 Å (VI)) hinder their incorporation into the oxide lattice [45].

However, successful incorporation does not depend solely on size. F^- also has electronegativity (3.98) and 2p orbital energy close to those of oxygen (3.44), which allows sufficient d–p overlap with Fe/Mn and maintains compatibility with the covalent TM–O framework. In contrast, Cl^- (3.16) and Br^- (2.96) have lower electronegativity and high-energy 3p/4p orbitals, which prevent effective hybridization. Furthermore, the stronger and thermally more robust TM—F bonds favor the incorporation of Funder solid-phase synthesis conditions, while the weaker TM—Cl and TM—Br bonds do not persist at high temperatures. Finally, due to its small size and higher mobility, F^- diffuses more easily through the oxide lattice, while the much larger Cl^- and Br^- ions must overcome significant kinetic barriers, which further hinder their incorporation.

However, even for the F^- by O^{2-} substitution only very low substitution levels are achieved, as we showed, which may be an effect of the aliovalent substitution that necessarily would need to be balanced by the transition metal valence change and/or a reduced thermodynamic stability of the desired P2 phase in favor of other phases, which is going to be explored in the next chapter.

2.4 | DFT Calculations

To further examine the effect of substitution toward stability of P2-NFMO, and confirm the secondary phases from QPA, simulation by means of DFT calculations has been utilized. Based on NFMO, two substitution concentrations $x = 0.03$ mol and $x = 0.06$ mol for A dopant (where A = F/Cl/Br) $Na_{0.67}Fe_{1/3}Mn_{2/3}O_{2-x}A_x$ were constructed to examine the trend in substituted concentration. First principles calculations were performed for NFMO and halide-substituted NFMO and all competing compounds in the Na–Fe–Mn–O–X system (see Table S8 in Supporting Information for the list of compounds), through the DFT method using the Vienna ab initio simulation package (VASP) [46]. The electron–ion interactions were modeled using the projector augmented wave method [47], while the electron–electron interactions are taken into account by the exchange-correlation function under the generalized gradient approximation (GGA) of Perdew–Burke–Ernzerhof [48]. Atomic coordinates were optimized until the Hellmann–Feynman force on each atom fell below 0.01 eVÅ^{-1}, and the total energy difference was less than 10^{-5} eV. Wave functions were represented using plane waves with a maximum energy cutoff of 520 eV, ensuring high accuracy. The *k*-point mesh was chosen at $5 \times 5 \times 2$ for the $3 \times 3 \times 2$ NFMO supercell in the Monkhorst–Pack scheme. To assess the stability of halide-substituted NFMO relative to other competing phases in the Na–Fe–Mn–O–X system, we utilized a self-developed MATLAB code [49–51]. The reaction energy E_r of the main phase (halide-substituted NFMO) against their possible competing phases was calculated according to the following equation:

$$E_r = E_f[\text{competing phases}] - E_f[\text{main phase}] \quad (2)$$

where E_f represents formation energy, the energy change when a compound is formed from its constituent elements in their standard state (Table S8, Supporting Information). In this study, the oxygen chemical potential was fixed at $\mu_O = -1.48$ eV based on the equation $\mu_O(T, P_{O_2}) = \frac{1}{2}\left\{\mu_{O_2}(T, P^O) + k_B T \ln \frac{P_{O_2}}{P^0}\right\}$, where $T = 1173$K, $P^O = 1$ atm, and $P_{O_2} = 0.21$ atm, facilitating better comparison with experimental results.

Various halide substitution arrangements at the O-sites were considered to identify the most stable configurations, as illustrated in Figure 4a. According to the thermodynamic conditions of halide-substituted P2-NFMO and the constraints imposed by stable compounds on the Na–Fe–Mn–O–X, the halide-substituted P2-NFMO equilibria are shown in Figure 4b and Table S9. The primary decomposition phase is P2- NFMO (around 95%), followed by NaBr/NaCl/NaF (around 3%) and small amounts of $MnBr_2$/$MnCl_2$/MnF_2, as well as TM-oxides ($MnFe_2O_4$, Fe_2O_3,Mn_2O_3, MnO_2, MnO, FeO) as listed in Table S9.

Multiple decomposition reactions are possible, with the lowest-energy decomposition phases representing the thermodynamic ground states. These are depicted by solid symbols in Figure 4b, while the dashed line marks the boundary between stable and unstable regions, as confirmed by experimental observations. However, QPA and DFT revealed larger instabilities in most halide-substituted samples with Na-halides and TM-oxides coexisting with the P2-phase. For P2-NFMO with 0.03 mol F^-, the decomposition energy is relatively low (−22.57 meV/atom) and is predicted to be even smaller at 0.02 mol substitution (around −13 meV/atom). Such small energy values suggest potential kinetic inhibition of decomposition, explaining why no decomposition phase was experimentally detected (PXRD/QPA) for the 0.02 F-substituted NFMO. The calculations further indicate that phase stability follows the trend F-substituted > Cl-substituted > Br-substituted, with decomposition energy becoming more negative as substitution concentration increases (Figure 4b, Table S9 in Supporting Information).

Moreover, the optimized structure in Figure 4a shows that Cl^-, and especially Br^-, shift away from the O^{2-} layer toward the Na layer, highlighting increased structural instability due to their larger atomic radii. Moreover, it was observed that even when

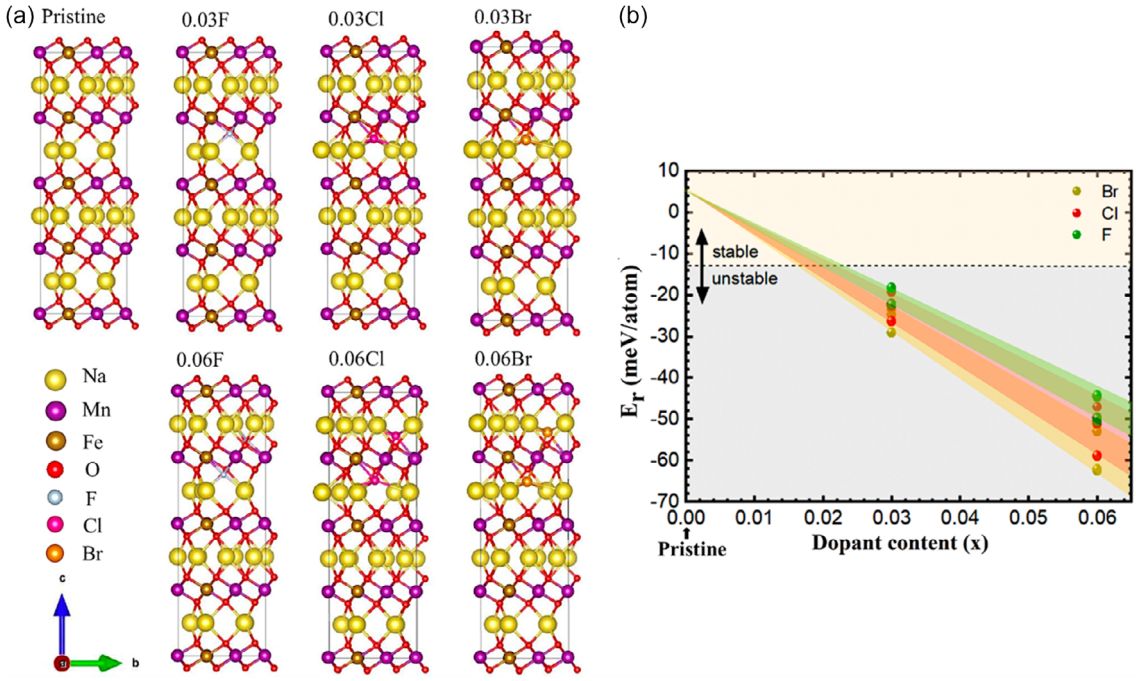

FIGURE 4 | Optimized atomistic structures of pristine NFMO and F/Cl/Br-substituted NFMO (a). DFT results of phase stability of F/Cl/Br-substituted NFMO (b).

$MnCl_2$ was used as a precursor, NaCl reformed (Figure S10, Supporting Information), confirming the unsuccessful Cl-substitution. The calculations further show that the decomposition energy is more negative for Br- than for Cl- substituted NFMO (Table S8, Supporting Information), indicating that Br^- destabilizes the P2 phase more significantly, which aligns with the larger amount of secondary phases observed for the Br^- series. DFT-calculated phase stabilities and QPA-quantified secondary phases correlate with halide ionic radius: the greater the difference between the halide and O^{2-} ionic radii, the less stable the P2-NFMO structure. Moreover, as the substitution concentration increases from 0.03 mol to 0.06 mol, the decomposition energy gets lower, and the products exhibit a reduction in P2-NFMO content and an increase in NaF/NaCl/NaBr content (Table S9, Supporting Information), consistent with the experimental observations.

2.5 | Electrochemical Performance

Electrochemical experiments were conducted to investigate the electrochemical characteristics of all samples. The cyclic voltammetry measurements were conducted in the range from 1.5 to 4 V versus Na/Na^+. Two distinct peaks occurring within this range, an oxidation peak referring to the reaction of $Mn^{3+}/Fe^{2+} \rightarrow Mn^{4+}/Fe^{3+}$ and a reduction peak referring to $Mn^{4+}/Fe^{3+} \rightarrow Mn^{3+}/Fe^{2+}$, were identified, Figure 5a–c. Mortemard de Boisse et al. [38] investigated the Fe/Mn redox pairs in P2-$Na_{0.66}Fe_{1/3}Mn_{2/3}O_2$ using Mössbauer spectroscopy, reporting the cation distribution $Na_{0.66}Fe^{3+}{}_{1/3}Mn^{3+}{}_{0.33}Mn^{4+}{}_{0.34}O_2$. They observed overlapping redox reactions from the Mn^{4+}/Mn^{3+} and Fe^{4+}/Fe^{3+} pairs when charged to 4.3 V. As the potential window in this study ranges up to 4 V, it can be assumed that the predominant redox pair is Mn^{3+}/Mn^{4+}, along with Fe^{2+}/Fe^{3}. This interpretation is supported by the broad oxidation and reduction features observed in the cyclic voltammetry (CV) measurements, which occur within the potential range where both redox pairs are electrochemically active [30, 52]. Given that no Mössbauer measurements were performed within this reduced potential window, it must be assumed at this stage that both Mn and Fe are involved in the electrochemical reaction.

The features of the CV curve remain unchanged at the lowest concentrations of F^- and Cl^- compared to NFMO. However, at the highest concentration, a noticeable change in the CV curve is observed, particularly for the F-substituted sample. Significant changes in the CV curve for the F-substituted sample occur at a concentration of 0.05 mol and are also noticeable at 0.1 (Figure S11, Supporting Information).

When integrating the CV curves within the potential ranges of 1.5–3.5 V and 3.5–4.0 V (as shown in Table S10 and Figure S12, Supporting Information), it becomes evident that the oxidation and reduction areas differ for all halide-substituted samples, with the oxidation area being larger than the reduction area. In contrast, all Br-substituted structures exhibit only minimal electrochemical activity (Figure S13, Supporting Information). Given that the oxidation and reduction areas differ and the oxidation/reduction peaks exhibit shifts, it can be assumed that the diffusion rates for intercalation and deintercalation are different. Additionally, irreversible phase transitions may also contribute to these observations [53, 54]. Moreover, changes in the shape of the oxidation and reduction curves in CV measurements at higher halide concentrations (Figures 5b,c, S11, Supporting Information) suggest that the presence of secondary phase, such as TM-oxides and Na halides, identified by PXRD/QPA, impacts the electrochemical activity and stability of P2-NFMO, thereby altering both curve profiles and areas.

For both concentrations of Br^-, only minimal electrochemical activity was observed (Figure S13). The low electrochemical

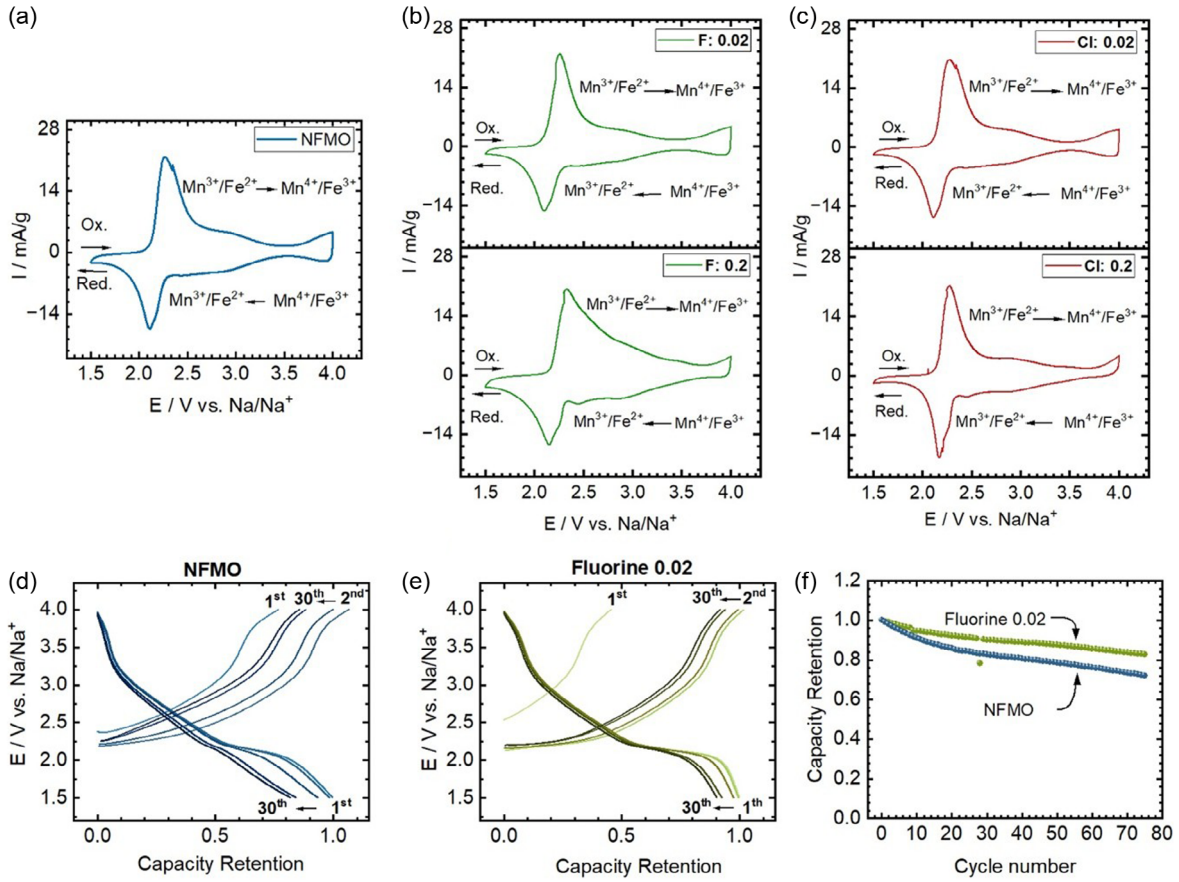

FIGURE 5 | Cyclic voltammogram of NFMO (a), 0.02 and 0.2 mol F-substituted NFMO (b) and 0.02 and 0.2 mol Cl-substituted NFMO (c). Galvanostatic charge/discharge of NFMO (d) and 0.02 mol F-substituted NFMO (e). Capacity retention vs cycle number of discharge capacities for NFMO and 0.02 mol F-substituted NFMO (f).

activity in the Br- substituted sample series can most likely be attributed to the significantly reduced P2 phase fraction and the formation of large secondary phases. The large ionic radius of Br^- favors these structural changes, which directly lead to a reduction in electrochemical activity. In addition, the Rietveld refinement shows a significant Na depletion in the remaining P2 phase, which further enhances the structural instability and deteriorates the electrochemical performance.

During the first charge cycle of the galvanostatic charge/discharge experiments (Figure 5d,e), both NFMO and the 0.02 mol F-substituted sample exhibit the lowest capacities. The specific capacities for both samples were determined (Figure S14, Supporting Information), but only capacity retention is shown in this section to highlight the differences in degradation behavior between the unsubstituted material and its F-substituted counterpart.

This initial low capacity is attributed to the initially high oxidation state of Mn, with $\approx 0.34\,Mn^{4+}$ present prior to charging. Within the applied potential window (1.5–4.0 V), the Mn^{3+}/Mn^{4+} and Fe^{2+}/Fe^{3+} couples dominate the redox activity. Consequently, only ~$0.33\,Mn^{3+}$ can be oxidized during the first charge, limiting the initial capacity. In the subsequent discharge, the full Mn^{3+}/Mn^{4+} redox couple becomes electrochemically accessible, enabling the recovery of full capacity [30, 55, 56]. Furthermore, these experiments show that the 0.02 mol F-substituted NFMO sample exhibits improved capacity retention compared to the unsubstituted NFMO. As shown in Figure 5f, the NFMO sample retains only 72% of its initial capacity after 75 cycles, whereas the 0.02 mol F-NFMO retains 83% of its initial capacity. The overall difference is about 15% higher capacity retention stability due to F-substitution. Moreover, the discharge curve of the F-substituted sample exhibits a longer plateau, suggesting a delayed phase transition, an effect not observed in NFMO.

Similar results were obtained in other studies. Liu et al. [33] showed that F-substitution in the P2-$Na_{2/3}Ni_{1/3}Mn_{2/3}O_{2-x}F_x$ ($x = 0$, 0.03, 0.05, 0.07) phase suppresses phase transitions in the low voltage range and improves electrochemical performance. Thus, demonstrating that F-substitution effectively stabilizes the structure. Similarly, Kang et al. [34] investigated F-substitution in P2-$Na_{0.60}Mn_{0.70}Ni_{0.3}O_{2-x}F_x$ ($x = 0$, 0.03, 0.05, and 0.07) and found that an optimal substitution concentration of $x = 0.05$ mol exhibited excellent rate capability and retained 78% of its capacity after 900 cycles. The superior performance was attributed to the increased diffusion coefficient of Na-ions and the improved charge transfer rate due to F-substitution. Our results strongly suggest that the observed improved electrochemical behavior is due to the effect of F-substitution, which increases covalency, in line with previous studies. This enforced binding energies through the incorporation of F^- could impact phase transitions from P2 to O2 during sodiation/desodiation, resulting in a more stable structure and thus improved cycling stability [57].

2.6 | *In Situ XRD*

To understand the incorporation of F^- into the P2 structure of NFMO and to investigate its impact on the structural evolution during sodiation and desodiation, *in situ* XRD measurements were performed in half-cells versus Na-metal, as shown in Figures 6a–d and S14 in Supporting Information. For both NFMO and the fluorinated sample NFMF0.02, the P2-type layered structure is maintained during desodiation up to 4.0 V and sodiation down to 1.5 V. During cycling, clear shifts in the (002), (004), (100), and (104) reflections are observed in both samples (Figure 6a,b), which are attributed to changes in the Mn oxidation state (Mn^{3+}/Mn^{4+}), leading to corresponding variations in ionic radii and lattice shrinkage due to desodiation.

Previous studies have reported the formation of a new orthorhombic phase (Cmcm, P′2-type) below 2 V during sodiation, indicated by a splitting of the (002) (100), (104), and (106) reflections due to the reduction of Mn^{4+} to Mn^{3+} [38, 55, 56]. In the present study, however, such splitting is only observed for (002) (Figure 6a/b). For (100) and (104), a decrease in intensity below 2 V is observed, which may indicate the onset of phase transformation. Notably, Ag Kα radiation ($\lambda = 0.56$ Å) was used in these measurements. The harder X-ray source leads to reflections appearing at lower 2θ angles, where peak overlap and smearing may obscure subtle splitting effects. Nonetheless, the intensity loss at 1.5 V suggests structural changes consistent with previously reported behavior [55, 56].

The evolution of the lattice parameters is shown in Figures 6a,b and S15 in the Supporting Information. The refined parameters of P2-NFMO/NFMF0.02 from the Rietveld refinement of the PXRD data were used as starting values for the lattice parameters. Reflections peak profiles of Al/Na were fitted considering preferred orientation and size effects in the first scans and then fixed for all subsequent scans. Strains, occupancies, and thermal Debye–Waller factors of P2- NFMO/NFMF0.02 kept constant. Only the lattice parameters a_{hex} and c_{hex}, as well as the size of P2-NFMO/NFMF, were refined to track a/c over multiple scans. To follow the evolution of the P`2 phase (Cmcm), the structure of $Na_{0.96}Fe_{1/3}Mn_{2/3}O_2$ (ICSD code 231008 [38]) was used as a reference.

The *a*-parameter decreases during desodiation, as Na^+ ions are extracted from the interlayer space and TM are oxidized from Mn^{3+} to Mn^{4+} and from Fe^{2+} to Fe^{3+}. This oxidation is associated with a reduction in ionic radii, leading to a contraction in the *a*-axis. Conversely, the *c*-parameter increases due to enhanced electrostatic repulsion between the TM layers upon Na^+ removal. A comparison of the lattice parameter changes reveals that the relative expansion of the *a*-axis as well as the *c*-axis is almost identical for NFMO and NFMF0.02, with 1.62% and 1.71% and 2.63%, and 2.69%, respectively. However, the phase transformation from P2 to Cmcm shows significant differences in kinetics for NFMO and NFMF0.02, as shown in Figure 6c,d. In NFMO, the P2 phase is almost completely converted to the Cmcm phase (P`2) after a single charge–discharge cycle. Whereas in NFMF0.02, about 30% of the P2-phase remains.

It is known that the Cmcm phase is formed during a deep discharge below 2 V, in which Mn^{4+} is reduced to high-spin Mn^{3+} with a $3d^4$ electron configuration. The one-electron occupation of the e_g orbital neutralizes the orbital degeneracy, leading to a Jahn–Teller distortion of the MnO_6 octahedral. This structural distortion leads to the transformation of the P2-phase into the orthorhombic Cmcm phase [55].

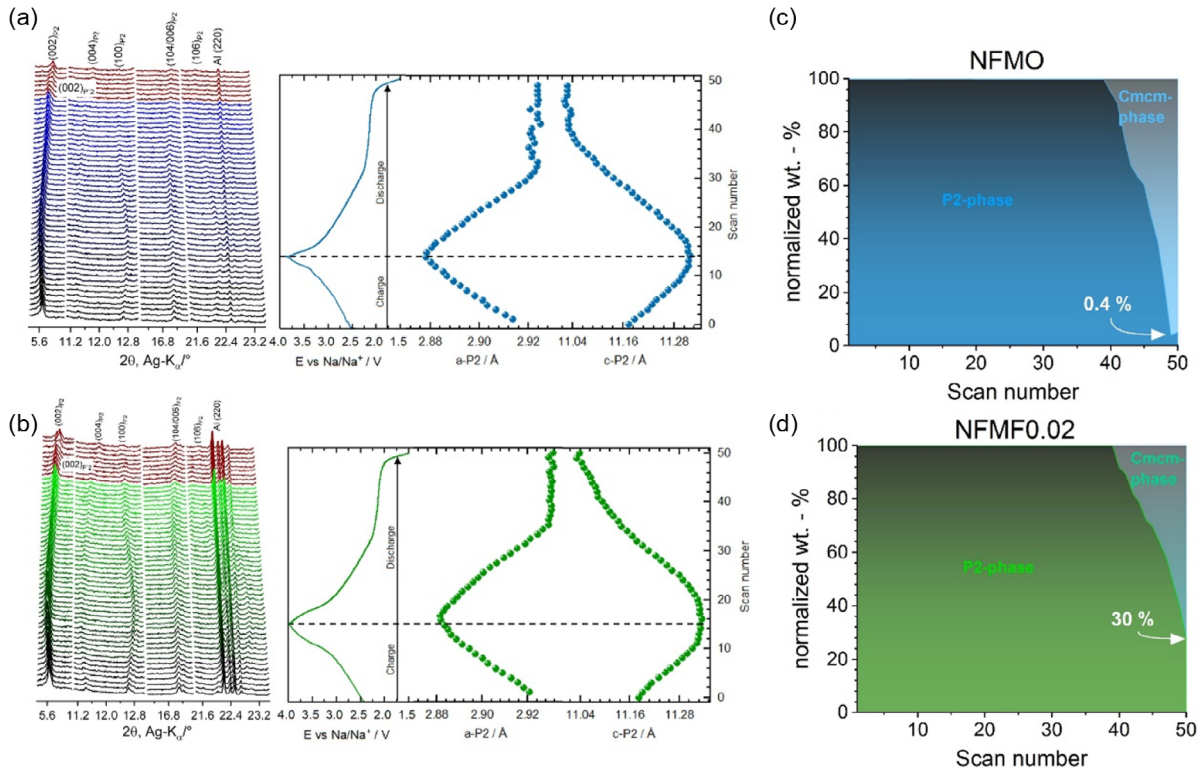

FIGURE 6 | In situ XRD measurements in half cells against Na metal at C/20 rate of NFMO (a) and NFMF0.02 (b) and determined changes of lattice parameter. Phase fraction of P2 and Cmcm-phase in NFMO (c) and NFMF0.02 (d).

The partial substitution of O^{2-} by F^- in the NFMO framework strengthens the F—TM bonds, delaying the formation of the Cmcm phase and thus leading to structural stabilization during cycling, as eventually evidenced from the quantitative analysis of our in situ PXRD data.

3 | Conclusion

This study investigated the feasibility of halide substitutions ($A = F^-$, Cl^-, Br^-) in P2-$Na_{0.66}Fe_{1/3}Mn_{2/3}O_{2-x}A_x$. The given synthesis conditions (solid-state reaction at elevated temperatures and times) were selected to yield samples in thermodynamic equilibrium. The successful incorporation of F-ions into the layered oxide P2-$Na_{0.66}Fe_{1/3}Mn_{2/3}O_2$ was achieved at a concentration of 0.02 mol per FU by a two-step solid-state reaction. For all other samples, the formation of secondary phases is observed in both Raman spectra and XRD patterns. QPA and DFT suggest that the P2 phase experiences a decreased thermodynamic stability in the presence of halides. Hence, instead of halide incorporation, simpler binary compounds are formed. For future material development, alternative synthesis strategies should be considered to enable the successful incorporation of halide ions such as Cl^- or Br^- into the P2-type layer structure. In particular, methods such as sol–gel synthesis or hydrothermal approaches could enable improved control over homogeneity, ion diffusion, and reaction kinetics, thereby facilitating the stabilization of halides within the LTMO lattice.

This study further revealed a solubility limit for F^- in the P2 phase of 0.035 mol as determined by Rietveld refinement and QPA. Raman spectroscopy provided additional evidence for the successful incorporation of F^- and showed a blueshift of the A_{1g} vibration and a broadening of the peak, indicating changes in bond strength. Electrochemical cycling analysis revealed a 15% improvement in capacity retention after 75 cycles for the F-substituted NFMO material. In situ XRD measurements revealed a different phase transformation mechanism in the low voltage range for NFMO and NFMF0.02. For NFMO, the P2-phase is completely transformed into Cmcm, whereas for NFMF0.02, 30% P2-phase remains, which stabilizes the structure and thus improves the electrochemical performance. Previous studies have demonstrated the advantages of F^- doping in terms of capacity, structural stability, and Na^+ conductivity, but they lack in situ phase quantification and focus mainly on Mn/Ni or O3-type NFM systems. Our study fills this gap by quantifying in situ XRD measurements of Fe/Mn-based P2 cathodes, thereby establishing a quantitative relationship between phase evolution and electrochemical behavior. This underlines the potential of F-substituted NFMO for practical implementation in next-generation, cost-effective sodium-ion battery systems.

4 | Experimental Section

4.1 | Synthesis

The P2-$Na_{0.66}Fe_{0.33}Mn_{0.66}O_2$ (NFMO), the F-substituted P2-$Na_{0.66}Fe_{0.33}Mn_{0.66}F_xO_{2-x}$ ($x = 0.02$, 0.05, 0.1, 0.2 mol), and the Cl/Br-substituted P2- $Na_{0.66}Fe_{0.33}Mn_{0.66}A_xO_{2-x}$ ($A = Cl$ or Br; $x = 0.02$, 0.2) were synthesized by a two-step solid-state reaction. Stoichiometric amounts of the precursors $Na_2CO_3 \cdot 10H_2O$ (Carl Roth, ≥99%), Fe_2O_3 (Alfa Aesar, 99%), MnO_2 (Carl Roth, ≥98%), NaF (Thermo Scientific, 99%), NaCl (Thermo Scientific, 99.5%), and NaBr (Honeywell, 99%) were thoroughly mixed using a mortar grinder (Retsch RM 200).

In the first synthesis step, the precursor mixtures were calcined at 800°C for 8 h in covered alumina crucibles, using a heating rate of 5 K min^{-1}. The resulting powders were then re-ground and pressed into pellets for a second high-temperature treatment. In the second step, the pellets were sintered at 900°C for 12 h under identical heating conditions.

After cooling, the sintered pellets were ground into fine powders and immediately transferred to an Ar-filled glovebox to prevent degradation due to moisture exposure.

4.2 | ICP-OES

The ICP-OES (Thermo Scientific, iCAP 7000 Series) was used for double-checking the stoichiometries of synthesized samples. 2 aliquots of 50 mg samples were dissolved in 3 mL HCl + 1 mL H_2O_2 at room temperature. Each solution was then made up to a total volume of 50 mL. 2 parallel dilutions of each digested solution (100-fold) were prepared for analysis. The evaluation was carried out by using a multi-element calibration.

4.3 | X-Ray Powder Diffraction

The PXRD patterns were recorded by a lab diffractometer (Empyrean, Panalytical) with a molybdenum anode (K_α wavelength 0.7107 Å). The measurements were carried out in a Bragg–Brentano geometry under a dome sample holder made of polyethylene (Malvern Panalytical) to protect the sample from humidity. All samples were measured in a 2θ range of 5°–80° with a step size of 0.0084°. The QPA based on the PXRD data were conducted by using the software package Diffrac.Topas Version 7 (Bruker). The crystallized size, strain, and lattice parameters were determined by using the Pawley method. Rietveld refinement analyses were performed for NFMO, 0.02 and 0.05 mol F-substituted and 0.02 mol Cl-substituted NFMO, for which the occupancies, thermal Debye–Waller factors, and scale factors were refined.

4.4 | SEM

SEM images were taken by Quanta FEG 650 FEI, USA. The powder samples were initially placed in a Kammrath & Weiss transfer vessel inside a glove box to protect them from contact with the ambient atmosphere. The images were obtained by using an accelerating voltage e-beam of 10 kV/20 kV equipped with a secondary electron detector.

4.5 | RBS

For the RBS, the powder samples were first pressed into pellets with a diameter of 11 mm. Because RBS measurements require a high relative density flat surface, these pellets were then sintered at 900°C for 12 h to obtain high relative density sample pellets and polished by using SiC sand papers to obtain flat surfaces for the measurements. The RBS was conducted using a

1461 keV proton beam. The data were collected at a scattering angle of 153° and an exit angle of 27°. The experimental results were simulated and analyzed by using the SIMNRA software [58].

4.6 | Raman Spectroscopy

Raman spectroscopy measurements were conducted with a WITEC alpha300R microscope using a solid-state 532 nm excitation laser. The spectra were recorded by using a 600 l/mm grating and 0.1 mW laser power. An area of 50 µm by 50 µm was mapped on each sample with a 50x objective and a step size of 1 µm. The recorded spectra were evaluated by a correction algorithm for cosmic ray removal and baseline correction. The processed spectra of NFMO, 0.02 Cl-, and 0.02 mol F-substituted NFMO were fitted with a Voigt function to determine the exact position of the bands. Starting values for the five expected bands ($E_{1g} + 3E_{2g} + A_{1g}$) were 166 cm^{-1}, 367 cm^{-1}, 459 cm^{-1}, 581 cm^{-1}, and 619 cm^{-1} [37]. The processed spectra of 0.02 and 0.2 mol Br-substituted, 0.2 mol Cl-substituted, and 0.2 mol F-substituted samples were analyzed using component analysis within the WITec software package. Subsequently, all identified components were fitted using a Voigt function.

4.7 | DFT Calculations

DFT calculations were performed using the VASP [46] to study NFMO, F-, Cl-, and mol Br-substituted NFMO and their competing compounds in the halide-doped Na–Fe–Mn–O system. The electron–ion interactions were modeled using the projector augmented wave method [47], while the electron–electron interactions are taken into account by the exchange-correlation function under the GGA of Perdew–Burke–Ernzerhof [48]. Atomic coordinates were optimized until the Hellmann–Feynman force on each atom fell below 0.01 $eVÅ^{-1}$, and the total energy difference was less than 10^{-5} eV. Wave functions were represented using plane waves with a maximum energy cutoff of 520 eV, ensuring high accuracy. The *k*-point mesh was chosen at $5 \times 5 \times 2$ for the $3 \times 3 \times 2$ NFMO supercell in the Monkhorst−Pack scheme. Reaction energies were computed using a custom MATLAB code, and the oxygen chemical potential was fixed at $\mu_O = -1.48$ eV to align with experimental conditions.

4.8 | Electrochemical Measurement

For the preparation of electrodes, the active materials were mixed with Polyvinylidene fluoride (PVDF) in a N-Methly-2-pyrrolidone (NMP) solution and carbon black (Super P, Alfa Aesar) with a weight ratio of 70:15:15. The slurry was cast by using a doctor blade onto the as purchased 12 µm thick aluminum foil (Carl–Roth). Initially, the tapes were dried on a heating plate at a temperature of 120°C for 1 h. Round shape cathode electrodes with a diameter of 11 mm were then punched out of the tapes and dried overnight under a high vacuum. The cathodes were tested electrochemically against Na-metal by combining Celgard 2500 and glass fiber separators (Whatman GF/D) and assembled in CR2032-type coin cells. 0.9 M $NaPF_6$ (Sigma–Aldrich, 98%) and 0.1 M $NaBF_4$ (Sigma–Aldrich, 98%) dissolved in diethylene glycol-dimethyl ether (Sigma–Aldrich, anhydrous 99.5%) were used as the electrolyte. The electrochemical tests were carried out using a BioLogic MPG-200 potentiostat equipped with a climate chamber. Every cycling protocol started with recording open circuit voltage for 24 h before other electrochemical tests were carried out. For NFMO, F- or Cl- substituted NFMO, CV experiments were carried out within a potential window of 1.5–4 V versus Na/Na^+ with a scanning rate of 0.02 mVs^{-1}. For NFMO and 0.02 mol F-substituted NFMO, galvanostatic charge/discharge were carried out at 0.05 C in a potential range of 1.5–4 V versus Na/Na^+.

4.9 | In Situ XRD

In situ XRD measurements were conducted using CR2032-type coin cells equipped with a cut aluminum foil window. The cathodes, composed of NFMO and NFMF0.02, were tested against Na-metal. A combination of Celgard 2500 and Whatman GF/D glass fiber was used as a separator material. The electrolyte consisted of 0.9 M $NaPF_6$ and 0.1 M $NaBF_4$ (both ≥98%, Sigma–Aldrich) dissolved in diethylene glycol dimethyl ether (diglyme, anhydrous, 99.5%, Sigma–Aldrich). Electrochemical measurements were performed using a BioLogic MPG-200 potentiostat. In situ XRD data were collected on a lab diffractometer (Empyrean, Malvern Panalytical) equipped with a silver anode ($K\alpha$, $\lambda = 0.56$ Å) in Debye–Scherrer geometry, covering a 2θ range of 3° to 30°.

Author Contributions

Anna Domgans: conceptualization (equal), data curation (lead), formal analysis (lead), investigation (equal), methodology (lead), validation (lead), visualization (lead), writing– original draft (lead), writing – review & editing (equal). **Ngoc Thanh Thuy Tran:** conceptualization (supporting), data curation (equal), formal analysis (equal), investigation (equal), methodology (equal), validation (supporting), visualization (supporting), writing – original draft (supporting), writing – review & editing (supporting). **Sebastian Speer:** formal analysis (supporting), methodology (supporting), validation (supporting), writing – original draft (supporting), writing – review & editing (supporting). **Asghar N Kayani:** data curation (supporting), formal analysis (supporting), investigation (supporting), methodology (supporting), validation (supporting), writing original draft (supporting), writing – review & editing (supporting). **Frederik Zantis:** formal analysis (supporting), investigation (supporting), methodology (supporting), writing – original draft (supporting). **Tobias Braun:** formal analysis (supporting), investigation (supporting), methodology (supporting), validation (supporting), writing – original draft (supporting), writing – review & editing (supporting). **Kristian Schaps:** data curation (supporting), formal analysis (supporting), investigation (supporting), methodology (supporting), writing – review & editing (supporting). **Chih-Long Tsai:** supervision (supporting), writing – original draft (supporting), writing review & editing (supporting). **Hermann Tempel:** project administration (supporting), resources (supporting), supervision (supporting), writing – original draft (supporting), writing – review & editing (supporting). **Luc Raijmakers:** project administration (supporting), resources (supporting), supervision (supporting), writing – original draft (supporting), writing – review & editing (supporting). **Shih-kang Lin:** methodology (supporting), project administration (supporting), resources (supporting), supervision (supporting), writing – original draft (supporting), writing – review & editing (supporting). **Anna Windmüller:** conceptualization (lead), funding acquisition (supporting), investigation (equal), methodology (equal), project administration (supporting), supervision (equal), writing – original draft (supporting), writing – review & editing (equal). **Rüdiger-A. Eichel:** resources (lead), supervision (equal), writing – original draft (supporting), writing – review & editing (supporting).

Acknowledgments

This work was financially supported by the project of "High Performance Solid-State Batteries." (HIPSTER) from "Ministerium für Kultur und Wissenschaft des Landes Nordrhein-Westfalen" from Bundesministerium für Bildung,und Forschung.

Open Access funding enabled and organized by Projekt DEAL.

Funding

This study was supported by Ministerium für Kultur und Wissenschaft des Landes Nordrhein-Westfalen.

Conflicts of Interest

The authors declare no conflicts of interest.

Data Availability Statement

Data related to this study are available in the repository at the following link: -https://doi.org/10.26165/JUELICH-DATA/C6G1FF.

References

1. P. Gupta, S. Pushpakanth, M. A. Haider, and S. Basu, "Understanding the Design of Cathode Materials for Na-Ion Batteries," *ACS Omega* 7 (2022): 5605, https://doi.org/10.1021/acsomega.1c05794.

2. X. Wang, S. Roy, Q. Shi, Y. Li, Y. Zhao, and J. Zhang, "Progress in and Application Prospects of Advanced and Cost-Effective Iron (Fe)-Based Cathode Materials for Sodium-Ion Batteries," *Journal of Materials Chemistry A* 9 (2021): 1938, https://doi.org/10.1039/D0TA10610K.

3. Y. E. Durmus, H. Zhang, F. Baakes, et al., "Side by Side Battery Technologies with Lithium-Ion Based Batteries," *Advanced Energy Materials* 10 (2020), https://doi.org/10.1002/aenm.202000089.

4. M. Baumann, M. Häringer, M. Schmidt, et al., "Prospective Sustainability Screening of Sodium-Ion Battery Cathode Materials," *Advanced Energy Materials* 12 (2022), https://doi.org/10.1002/aenm.202202636.

5. Z. Dai, U. Mani, H. T. Tan, and Q. Yan, "Advanced Cathode Materials for Sodium-Ion Batteries: What Determines Our Choices?" *Small Methods* 1 (2017), https://doi.org/10.1002/smtd.201700098.

6. H. Kim, "Sodium-Ion Battery: Can It Compete with Li-Ion?" *ACS Materials Au* 3 (2023): 571, https://doi.org/10.1021/acsmaterialsau.3c00049.

7. B. Sayahpour, H. Hirsh, S. Parab, L. H. B. Nguyen, M. Zhang, and Y. S. Meng, "Perspective: Design of Cathode Materials for Sustainable Sodium-Ion Batteries," *MRS Energy and Sustainability : A Review Journal* 9 (2022): 183, https://doi.org/10.1557/s43581-022-00029-9.

8. W. Tang, X. Song, Y. Du, et al., "High-Performance $NaFePO_4$ Formed by Aqueous Ion-Exchange and Its Mechanism for Advanced Sodium Ion Batteries," *Journal of Materials Chemistry A* 4 (2016): 4882, https://doi.org/10.1039/C6TA01111J.

9. S. Bublil, M. Fayena-Greenstein, M. Talyanker, et al., "Na-Ion Battery Cathode Materials Prepared by Electrochemical Ion Exchange from Alumina-Coated $Li_{1+x}Mn_{0.54}Co_{0.13}Ni_{0.1+y}O_2$," *Journal of Materials Chemistry A* 6 (2018): 14816, https://doi.org/10.1039/C8TA05068F.

10. J.-Y. Hwang, S.-T. Myung, and Y.-K. Sun, "Sodium-Ion Batteries: Present and Future," *Chemical Society Reviews* 46 (2017): 3529, https://doi.org/10.1039/c6cs00776g.

11. E. Goikolea, V. Palomares, S. Wang, et al., "Na-Ion Batteries—Approaching Old and New Challenges," *Advanced Energy Materials* 10 (2020), https://doi.org/10.1002/aenm.202002055.

12. T. Jin, H. Li, K. Zhu, P.-F. Wang, P. Liu, and L. Jiao, "Polyanion-Type Cathode Materials for Sodium-Ion Batteries," *Chemical Society Reviews* 49 (2020): 2342, https://doi.org/10.1039/c9cs00846b.

13. R. Usiskin, Y. Lu, J. Popovic, et al., "Fundamentals, Status and Promise of Sodium-Based Batteries," *Nature Reviews Materials* 6 (2021): 1020, https://doi.org/10.1038/s41578-021-00324-w.

14. A. Paolella, C. Faure, V. Timoshevskii, et al., "A Review on Hexacyanoferrate-Based Materials for Energy Storage and Smart Windows: Challenges and Perspectives," *Journal of Materials Chemistry A* 5 (2017): 18919, https://doi.org/10.1039/C7TA05121B.

15. A. Rudola, K. Du, and P. Balaya, "Monoclinic Sodium Iron Hexacyanoferrate Cathode and Non-Flammable Glyme-Based Electrolyte for Inexpensive Sodium-Ion Batteries," *Journal of the Electrochemical Society* 164 (2017): A1098–A1109, https://doi.org/10.1149/2.0701706jes.

16. B. Peng, Z. Zhou, J. Shi, X. Huang, Y. Li, and L. Ma, "Earth-Abundant Fe-Mn-Based Compound Cathodes for Sodium-Ion Batteries: Challenges and Progress," *Advanced Functional Materials* (2024): 34, https://doi.org/10.1002/adfm.202311816.

17. P. Li, T. Yuan, J. Qiu, et al., "A Comprehensive Review of Layered Transition Metal Oxide Cathodes for Sodium-Ion Batteries: The Latest Advancements and Future Perspectives," *Materials Science and Engineering: R: Reports* 163 (2025): 100902, https://doi.org/10.1016/j.mser.2024.100902.

18. T. Chen, B. Ouyang, X. Fan, W. Zhou, W. Liu, and K. Liu, "Oxide Cathodes for Sodium-Ion Batteries: Designs, Challenges, and Perspectives," *Carbon Energy* 4 (2022): 170, https://doi.org/10.1002/cey2.153.

19. C. Delmas, C. Fouassier, and P. Hagenmuller, "Structural Classification and Properties of the Layered Oxides," *Physica* 99B (1980): 81.

20. H. Yang, D. Wang, Y. Liu, et al., "Improvement of Cycle Life for Layered Oxide Cathodes in Sodium-Ion Batteries," *Energy and Environmental Science* 17 (2024): 1756, https://doi.org/10.1039/D3EE02934D.

21. Y.-J. Guo, R.-X. Jin, M. Fan, et al., "Sodium Layered Oxide Cathodes: Properties, Practicality and Prospects," *Chemical Society Reviews* 53 (2024): 7828, https://doi.org/10.1039/d4cs00415a.

22. Y. Liu, Y.-H. Zhang, J. Ma, J. Zhao, X. Li, and G. Cui, "Challenges and Strategies toward Practical Application of Layered Transition Metal Oxide Cathodes for Sodium-Ion Batteries," *Chemistry of Materials* 36 (2024): 54, https://doi.org/10.1021/acs.chemmater.3c02115.

23. H.-R. Yao, L. Zheng, S. Xin, and Y.-G. Guo, "Air-Stability of Sodium-Based Layered-Oxide Cathode Materials," *Science China Chemistry* 65 (2022): 1076, https://doi.org/10.1007/s11426-022-1257-8.

24. M. Li, W. Lin, Y. Ji, et al., "Recent Progress in High-Voltage P2-Na_x TMO_2 Materials and Their Future Perspectives," *RSC Advances* 14 (2024): 24797, https://doi.org/10.1039/d4ra04790g.

25. J. H. Stansby, N. Sharma, M. Avdeev, et al., "Dopant and Current Rate Dependence on the Structural Evolution of P2-$Na_{2/3}Mn_{0.8}Zn_{0.1}M_{0.1}O_2$ (M =Cu, Ti): An Operando Study," *Chemistry Methods* 1 (2021): 295, https://doi.org/10.1002/cmtd.202000075.

26. Z. Yan, L. Tang, Y. Huang, et al., "A Hydrostable Cathode Material Based on the Layered P2@P3 Composite that Shows Redox Behavior for Copper in High-Rate and Long-Cycling Sodium-Ion Batteries," *Angewandte Chemie (International ed., in English)* 58 (2019): 1412, https://doi.org/10.1002/anie.201811882.

27. Z. Yuan, W. Xuehang, W. Wenwei, and W. Kaituo, "Synthesis and Electrochemical Performance of $Na_{0.7}Fe_{0.7}Mn_{0.3}O_2$ as a Cathode Material for Na-Ion Battery," *Ceramics International* 40 (2014): 13679, https://doi.org/10.1016/j.ceramint.2014.04.126.

28. J. S. Thorne, R. A. Dunlap, and M. N. Obrovac, "Structure and Electrochemistry of $NaxFexMn_{1-x}O_2$ ($1.0 \leq x \leq 0.5$) for Na-Ion Battery Positive Electrodes," *Journal of the Electrochemical Society* 160 (2012): A361–A367, https://doi.org/10.1149/2.058302jes.

29. N. Yabuuchi, M. Kajiyama, J. Iwatate, et al., "P2-Type $Na_{(x)}Fe_{(1/2)}Mn_{(1/2)}O_2$ Made from Earth-Abundant Elements for Rechargeable Na Batteries," *Nature Materials* 11 (2012): 512, https://doi.org/10.1038/nmat3309.

30. J. Zhao, J. Xu, D. H. Lee, N. Dimov, Y. S. Meng, and S. Okada, "Electrochemical and Thermal Properties of P2-Type $Na_{2/3}Fe_{1/3}Mn_{2/3}O_2$ for Na-Ion Batteries," *Journal of Power Sources* 264 (2014): 235, https://doi.org/10.1016/j.jpowsour.2014.04.048.

31. J. Wang, Y.-F. Zhu, Y. Su, et al., "Routes to High-Performance Layered Oxide Cathodes for Sodium-Ion Batteries," *Chemical Society Reviews* 53 (2024): 4230, https://doi.org/10.1039/d3cs00929g.

32. Y. Cao, M. Xiao, X. Sun, W. Dong, and F. Huang, "Recent Advances on High-Capacity Sodium Manganese-Based Oxide Cathodes for Sodium-Ion Batteries," *Chemistry – A European Journal* 29 (2023): e202202997, https://doi.org/10.1002/chem.202202997.

33. K. Liu, S. Tan, J. Moon, et al., "Insights into the Enhanced Cycle and Rate Performances of the F-Substituted P2-Type Oxide Cathodes for Sodium-Ion Batteries," *Advanced Energy Materials* 10 (2020), https://doi.org/10.1002/aenm.202000135.

34. W. Kang, P. Ma, Z. Liu, et al., "Tunable Electrochemical Activity of P2-$Na_{0.6}Mn_{0.7}Ni_{0.3}O_{2-x}F_x$ Microspheres as High-Rate Cathodes for High-Performance Sodium Ion Batteries," *ACS Applied Materials and Interfaces* 13 (2021): 15333, https://doi.org/10.1021/acsami.1c02216.

35. B. K. Ganesan and Y.-S. Lee, "Phase Transition Induced Enhanced Performance of Sodium-Rich $Na_{1.2}Mn_{0.8}O_{2-\ y}F_y$ (y = 0-0.5) Cathodes," *ACS Applied Energy Materials* 6 (2023): 960, https://doi.org/10.1021/acsaem.2c03391.

36. Y.-S. Xu, M.-Y. Qi, Q.-H. Zhang, et al., "Anion Doping for Layered Oxides with a Solid-Solution Reaction for Potassium-Ion Battery Cathodes," *ACS Applied Materials and Interfaces* 14 (2022): 13379, https://doi.org/10.1021/acsami.2c00811.

37. G. Singh, J. M. D. L. Amo, M. Galceran, S. Pérez-Villar, and T. Rojo, "Structural Evolution during Sodium Deintercalation/Intercalation in $Na_{2/3}[Fe_{1/2}Mn_{\ 1/2}]O_2$," *Journal of Materials Chemistry A* 3 (2015): 6954, https://doi.org/10.1039/C4TA06360K.

38. B. M. de Boisse, D. Carlier, M. Guignard, et al., "Influence of Mn/Fe Ratio on Electrochemical and Structural Properties of P2-$NaxMn_{1-}yFe_yO_2$ Phases as Positive Electrode Material for Na-Ion Batteries," *Chemistry of Materials* 30 (2018): 7672, https://doi.org/10.1021/acs.chemmater.8b02953.

39. S. Hayashi, K. Mizumoto, S. Yoneda, Y. Kondo, H. Tanei, and S. Ukai, "The Mechanism of Phase Transformation in Thermally-Grown FeO Scale Formed on Pure-Fe in Air," *Oxide Metal* 81 (2014): 357, https://doi.org/10.1007/s11085-013-9442-7.

40. G. S. Pawley, "EDINP, the Edinburgh Powder Prot'de Refinement Program," *Journal of Applied Crystallography* (1980).

41. H. Wang, A. M. Hashem, A. E. Abdel-Ghany, et al., "Effect of Cationic (Na^+) and Anionic (F-) Co-Doping on the Structural and Electrochemical Properties of $LiNi_{1/3}Mn_{1/3}Co_{1/3}O_2$ Cathode Material for Lithium-Ion Batteries," *International Journal of Molecular Sciences* 23 (2022): 6755, https://doi.org/10.3390/ijms23126755.

42. M. Michalska, D. A. Ziółkowska, J. B. Jasiński, et al., "Improved Electrochemical Performance of $LiMn_2O_4$ Cathode Material by Ce Doping," *Electrochimica Acta* 276 (2018): 37, https://doi.org/10.1016/j.electacta.2018.04.165.

43. J. R. Hardy, A. M. Karo, I. W. Morrsion, C. T. Sennett, and J. P. Russell, "Lattice Dynamics and Second-Order Raman Spectrum of NaF".

44. B. K. Srivastava, D. P. Khandelwal, and H. D. Bist, "Raman Scattering and Vibrational Dynamics of $MnCl_2 \cdot 2H_2O$," *Journal Raman Spectroscopy* 7 (1978): 202, https://doi.org/10.1002/jrs.1250070408.

45. V. M. Goldschmidt, "The Principles of Distribution of Chemical Elements in Minerals and Rocks," *RSC* (1937): 655–637.

46. G. Kresse and D. Joubert, "From Ultrasoft Pseudopotentials to the Projector Augmentedwave Method," *Physical Review B* (1999).

47. P. E. Blochl, "Projector Augmented-Wave Method," *APS* (1994).

48. J. P. Perdew and K. Burke, "* Matthias Ernzerhof. "Generalized Gradient Approximation Made Simple," *APS* (1996).

49. C. Tsai, N. T. Thuy Tran, R. Schierholz, et al., "Instability of Ga-Substituted $Li_7La_3Zr_2O_{12}$ toward Metallic Li," *Journal of Materials Chemistry A* 10 (2022): 10998, https://doi.org/10.1039/D1TA10215J.

50. M. Ihrig, M. Finsterbusch, C.-L. Tsai, et al., "Low Temperature Sintering of Fully Inorganic All-Solid-State Batteries – Impact of Interfaces on Full Cell Performance," *Journal of Power Sources* 482 (2021): 228905, https://doi.org/10.1016/j.jpowsour.2020.228905.

51. C.-C. Wang, W.-C. Hsu, C.-Y. Chang, et al., "Grain Boundary Complexion Modification for Interface Stability in Garnet Based Solid-State Li Batteries," *Journal of Power Sources* 602 (2024): 234394, https://doi.org/10.1016/j.jpowsour.2024.234394.

52. I. Moeez, D. Susanto, W. Chang, H.-D. Lim, and K. Y. Chung, "Artificial Cathode Electrolyte Interphase by Functional Additives toward Long-Life Sodium-Ion Batteries," *Chemical Engineering Journal* 425 (2021): 130547, https://doi.org/10.1016/j.cej.2021.130547.

53. R. B. Smith, E. Khoo, and M. Z. Bazant, "Intercalation Kinetics in Multiphase-Layered Materials," *Journal of Physical Chemistry C* 121 (2017): 12505, https://doi.org/10.1021/acs.jpcc.7b00185.

54. Y. Zeng and M. Z. Bazant, *Phase Separation Dynamics in Isotropic Ion-Intercalation Particles*, 2013.

55. T. Yang, Y. Huang, J. Zhang, et al., "Insights into Ti Doping for Stabilizing the $Na_{2/3}Fe_{1/3}Mn_{2/3}O_2$ Cathode in Sodium Ion Battery," *Journal of Energy Chemistry* 73 (2022): 542, https://doi.org/10.1016/j.jechem.2022.06.016.

56. G. Zhang, J. Li, Y. Fan, et al., "Suppressed P2-P2′ Phase Transition of Fe/Mn-Based Layered Oxide Cathode for High-Performance Sodium-Ion Batteries," *Energy Storage Materials* 51 (2022): 559, https://doi.org/10.1016/j.ensm.2022.06.045.

57. H. Wang, L. Zhou, Z. Cheng, L. Liu, Y. Wang, and T. Du, "Recent Advances on F-Doped Layered Transition Metal Oxides for Sodium Ion Batteries," *Molecules* 28 (2023): 8065, https://doi.org/10.3390/molecules28248065.

58. M. Mayer, *AIP Conference Proceedings, AIP*, (1999), 541.

Supporting Information

Supporting Fig. S1: SEM images of 0.05 F-substituted (a), 0.1 F-substituted (b), 0.2 F-substituted, 0.2 Cl-substituted (d) and 0.2 Br-substituted NFMO. **Supporting Fig. S2:** EDS mappings from P2-$Na_{0.66}Fe_{1/3}Mn_{2/3}O_{2-x}$ Ax with A = F^-, Cl^-, Br^-; x = 0.02, 0.05, 0.1, 0.2 mol. **Supporting Fig. S3:** Logarithmic plot of PXRD-pattern from P2-$Na_{0.66}Fe_{0.33}Mn_{0.66}O_2$. **Supporting Fig. S4:** Rietveld refinement of NFMO (a) and 0.02 mol Br-substituted NFMO (b).**Supporting Fig. S5:** Rietveld-refinement analysis of 0.05 F-substituted (a), 0.1 F-substituted (b), 0.2 F-substituted (c), 0.2 Cl-substituted (d) and 0.2 Br-substituted (e) NFMO. **Supporting Fig. S6**: TM-O distance versus Na stoichiometry for NFMO, F-, Cl- and Br-substituted NFMO. **Supporting Fig. S7:** Lattice parameter a versus Na stoichiometry determined by Rietveld-refinement analysis (a) and QPA (b). Lattice parameter c versus Na stoichiometry determined by Rietveld-refinement analysis (c) and QPA (d). **Supporting Fig. S8:** RBS results of 0.05-substituted sample (a) and enlargement of the diagram (b). SIMNRA results of 0. mol -substituted sample (a) and enlargement of the diagram (d). **Supporting Fig. S9:** Raman spectra obtained from the component analysis

for 0.2 F-substituted structure (a) Raman spectra obtained from the component analysis for 0.2 Cl-substituted (b) and Br-substituted NFMO (c). **Supporting Fig. S10:** PXRD in logarithmic scale of 0.02 Cl-substituted sample. **Supporting Fig. S11:** CV measurement of 0.05 and 0.1 F-substituted NFMO. **Supporting Fig. S12:** Subdivided areas in CV for integration. **Supporting Fig. S13**: CV measurement of 0.02 and 0.2 Br-substituted NFMO. **Supporting Fig. S14:** GCPL measurements in half cells against Na-metal between 1.5 and 4.0 V with 0.05 C-rate for NFMO (a) and NFMF0.02 (b). **Supporting Fig. S15:** Determined lattice parameter P2 and Cmcm for NFMO (a) and NFMF0.02 (b). **Supporting Table S1**: Determined elements and obtained stoichiometry from ICP-OES analysis. **Supporting Table S2**: Rietveld-refinement parameter of P2-$Na_{0.66}Fe_{1/3}Mn_{2/3}O_2$. **Supporting Table S3:** Rietveld-refinement parameter of 0.02 F-substituted NFMO. **Supporting Table S4:** Rietveld-refinement parameter of 0.02 Cl-substituted NFMO. **Supporting Table S5**: Rietveld-refinement parameter of 0.05 F-substituted NFMO. **Supporting Table S6:** Results of QPA of 0.02 Br-substituted and 0.1 F-substituted and 0.2 F/Cl/Br-substituted P2-$Na_{0.66}Fe_{1/3}Mn_{2/3}O_{2.}$ **Supporting Table S7**: Phase fractions from QPA. **Supporting Table S8:** Calculated formation energies of possible competing phases of Na–Fe–Mn–O–F–Cl–Br at 0 K. **Supporting Table S9:** Decomposition phases and corresponding energies of F/Cl/Br-doped NFMO at and near ground states. **Supporting Table S10:** Calculated area of CV measurements.